

## ARTICLE

# Steel fiber reinforced concrete tensile testing with eliminated lateral wall effect

Katharina Look  | Peter Mark 

Institute of Concrete Structures, Faculty of Civil and Environmental Engineering, Ruhr University Bochum, Bochum, Germany

## Correspondence

Katharina Look and Peter Mark, Institute of Concrete Structures, Faculty of Civil and Environmental Engineering, Ruhr University Bochum, Universitätsstraße 150, 44801 Bochum, Germany.  
Email: [katharina.look@rub.de](mailto:katharina.look@rub.de) and [peter.mark@rub.de](mailto:peter.mark@rub.de)

## Abstract

A test rig and a novel experimental procedure are introduced and qualified to obtain realistic tensile strength of steel fiber reinforced concrete specimen with supercritical fiber contents from direct tensile tests. To eliminate the wall effect an optimal shape is found employing the method of tension triangles that ensures uniformly distributed stresses throughout. By water jet cutting an initially rectangular casted specimen is tapered at the center. The resulting bone-shaped specimen replicates the true manufacturing conditions of the component regarding fiber distribution and orientation. Accuracy of load introduction and surface quality are monitored tracking eccentricities and slip. Both are found strictly limited and without impact on the maximum experimental residual tensile strength of 2.87 MPa on average with a low scatter of 15%. Employing flexural bending tests from the same concrete batch, a conversion factor to the direct tensile test of  $\beta = 0.38$  was found for the first time.

## KEYWORDS

deflection-hardening, modularization, precast concrete members, rapid flow production, SFRC, steel fiber reinforced concrete, tensile testing, wall effect, water jet cutting

## 1 | INTRODUCTION

The continuing growth in the world's population is accompanied by a strong need for increased construction volumes. Voices for fast, efficient, and ecologically sustainable construction processes are becoming louder and louder as the lack of resources grow. New construction processes are needed to meet these demands. A decisive step in this direction can be the quality-robust series prefabrication of reinforced concrete components.<sup>1,2</sup>

However, the cost of placing reinforcement remains high. Steel fiber reinforced concrete (SFRC) has been used for a long time in industrial floor construction,<sup>3,4</sup> fire protection,<sup>5</sup> or as segmental reinforcement in mechanized tunneling<sup>6–11</sup> but mostly in combination with conventional rebar. At sufficiently high load bearing capacities, that is, at supercritical fiber contents and strengthening material behavior in the postcracking domain, steel fibers can substitute reinforcement holistically.<sup>12–16</sup> Waiving reinforcement work shortens processes in the precast industry. In plate-like components, the steel fibers distribute two-dimensionally<sup>17</sup> and form a full-surface reinforcement mesh that can replace crosswise laid reinforcing bars or mats. Precast flat elements with limited depth can be produced in any size

Discussion on this paper must be submitted within two months of the print publication. The discussion will then be published in print, along with the authors' closure, if any, approximately nine months after the print publication.

This is an open access article under the terms of the [Creative Commons Attribution](https://creativecommons.org/licenses/by/4.0/) License, which permits use, distribution and reproduction in any medium, provided the original work is properly cited.

© 2022 The Authors. *Structural Concrete* published by John Wiley & Sons Ltd on behalf of International Federation for Structural Concrete.

with consistent quality and completed at the installation site with in situ concrete to form a full-fledged component. Potential areas of application are, for example, in the production of individual foundations, element walls, or as components of a partial formwork replacement. On the way there, it must first be ensured that the load-bearing capacity of the SFRC is sufficient with a low degree of scatter. For this purpose, fiber contents have already been increased up to  $140 \text{ kg/m}^3$  (1.78 vol.-%) and residual flexural tensile strength of 8 MPa has been verified in Look et al.<sup>17</sup>

Common beam tests to determine the residual tensile strength from the residual flexural tensile strength via conversion factors are inexpensive and require little effort, but do not reflect the fiber orientation and distribution and cannot correctly reflect tensile load-bearing capacities. The direct determination via tensile test specimens is used almost exclusively for research due to the complex handling.<sup>18–20</sup> The more brittle the behavior, that is, with increasing the compressive strength of the concrete up to ultra-high performance concrete (UHPC) is, the higher the requirements on the stiffness of the testing machine are. RILEM was one of the few institutions to publish a standardized tensile test for steel fiber reinforced concrete as part of the TC162-TDF recommendations in 2001.<sup>21</sup> The well-established geometries of tensile test specimens such as cylinders influence the homogeneity and orientation of the fibers and thus the measured tensile strength.<sup>20</sup> Wille et al.<sup>20</sup> gives an overview of the specimen's shape, material, and attachment to the load introduction. Specimens without a defined tensile zone crack at an arbitrary location so that the stress–crack opening relationship cannot be reliably measured. Notches, on the other hand, facilitate the measurement of the crack opening but prevent the measurement of the centric tensile strength due to occurring notch stresses.<sup>22</sup> This can be circumvented by using a bone shape with a constant measuring range.<sup>23</sup> Stress peaks due to overly simplified tapers then often lead to unwanted failure outside the measurement range.<sup>24</sup> Geometries that are too small and do not match the fiber dimensions promote the wall effect and thus artificially increase the load-bearing capacity. These factors must be eliminated to gain realistic tensile strengths matching the component.

Equally important is the adjustment of the specimen to the load introduction. If this is done via glued joints, careful selection of the adhesive is essential, otherwise, the glued joint will fail before the specimen.<sup>21</sup> Clamping must be carried out without constraint and misalignment, as unwanted bending influences the results.<sup>23</sup>

For the here presented direct tensile tests bone-shaped specimens without a notch are used. This allows the stress–crack opening relationship to be recorded over

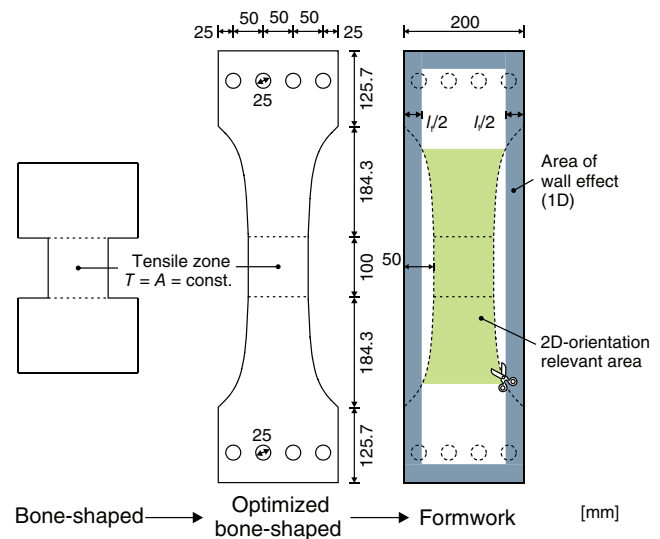


FIGURE 1 Geometry of the simple and optimized bone-shaped specimen for tensile testing

a constant measuring length. To get the optimum shape without stress peaks in the tapering, the specimens are shape-optimized and post-processed using the waterjet cutting technique. The elimination of the lateral wall effect achieved this way, which leads to one-dimensional fiber orientation, combined with the exploitation of favorable casting directions, yields a true two-dimensional fiber orientation as characteristic for flat components.<sup>25–27</sup> The result is a realistic tensile strength that can be used for the design of flat precast elements for the substitution of reinforcing steel.

## 2 | SPECIMENS' DESIGN

### 2.1 | Idea

The careful determination of strengths on small-scale material specimens to transfer them to real-scale components plays a crucial role in the safe and economical design of structures. The residual tensile strength of SFRC is primarily influenced by fiber orientation and distribution.<sup>28,29</sup> Both are influenced by the geometry, especially the concreting height, the manufacturing conditions, and consequently may not differ significantly in the tensile specimen from those of the real component. In the remainder, plane fiber orientation is ensured by restricting the depth of the specimen to 10 cm and employing horizontal concreting.<sup>17,30</sup>

To prevent failure in the load introduction zones of the specimen and to ensure a defined gauge length to detect the crack opening, a bone shape with a constant tensile zone at the center is selected, where the cross-

section  $A$  and therefore the tensile stress  $T$  is constant (Figure 1, left). Stress peaks and thus predetermined points of failure are avoided by tapering the cross-section using the method of tension triangles according to Mattheck et al.<sup>31,32</sup> based on the computer-aided optimization (CAO)<sup>33</sup> (Figure 1, center). This method adapts the biological growth rule originating from bionics according to Mattheck et al.<sup>34,35</sup> to the shape optimization of mechanical structures (Section 2.2). However, the specimens are initially concreted rectangular shaped (Figure 1, right). Using the waterjet cutting technique, the region where the so-called lateral wall effect<sup>3,36–39</sup> occurs is subsequently cut off (Figure 1, right, blue shaded). This region is assumed to run circumferentially at a distance of half the fiber length  $l_f/2$  from the inner edge of the formwork.<sup>38,39</sup> There, one-dimensional fiber orientation dominates in the direction of force, which can increase the tensile strength. From the 6 cm, long steel fiber minimum cut-off length of 3 cm is derived (Figure 1). For comparability of flexural to tensile tests, the concrete mix design from Look et al.<sup>17</sup> is used, with a fiber content of 140 kg/m<sup>3</sup> (1.78 vol.-%) using the high-strength fiber Dramix<sup>®</sup> 5D 65/60BG from NV Bekaert SA.

The load is introduced into the specimen via clamping and friction. For this purpose, the four circular openings ( $d_a = 25$  mm) in Figure 1 are used to accommodate threaded rods (M16-10.6). More details on the force application and its design can be found in Section 3.2 (cf. Figure 4). Compaction is performed externally by means of a vibrating table in order not to disturb fiber orientation and distribution. In parallel, three cubes are made to determine the compressive strengths on the test day. After 24 h, the specimens are stripped and stored in air at  $\sim 20^\circ\text{C}$  until the test day.

In order to measure realistic tensile strengths, the constant tensile zone must lie in the region of plane fiber orientation (green shaded). At the sides, the zone of one-dimensional fiber orientation, and thus the lateral wall effect, is eliminated by water jet cutting. Over the height, this wall effect is eliminated by a steady tapering of the cross-section over about 20 cm around the specimen center. This is sufficient to cause the crack zone in the region of plane fiber orientation. By contrast, the two-dimensional fiber orientation caused by the casting direction is not eliminated, since the specimen is intended to represent the load-bearing behavior of a flat component.

## 2.2 | Shaping

The biological growth rule according to Mattheck<sup>34</sup> is based on the axiom of constant stresses. It is inspired by the natural growth of biological items such as trees or

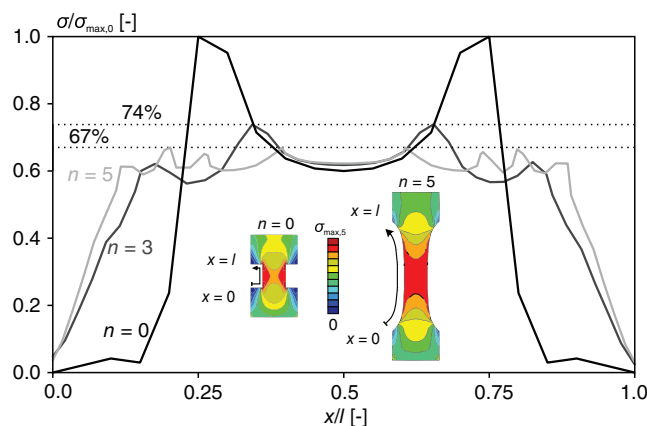


**FIGURE 2** Stress distribution in the specimens and utilization along the cutting edge

bones.<sup>40,41</sup> The basic principle is the accumulation of material at highly stressed locations and the removal of material at less stressed locations, which results in uniform stress. The CAO method adapts this rule to mechanical structures by creating artificial temperature strains at nodes until uniform loading is iteratively achieved.<sup>41</sup>

A graphical method for shape optimization has been derived from the CAO method, the method of tension triangles.<sup>31,32</sup> Its advantage is that it provides almost identically accurate reductions of notch stresses completely without numerical simulations using Finite Elements.<sup>42</sup>

Figure 2 compares the stress diagrams related to the associated cutting length  $l$  before ( $n = 0$ , black) and after  $n = 3$  (dark gray) as well as  $n = 5$  optimization steps (light gray). The indicated utilization is related to the maximum stress  $\sigma_{\max,0}$  of the initial specimen ( $n = 0$ ). Obviously, optimization yields a more homogeneous distribution with smaller gradients between the reduced stress peaks. After  $n = 3$  optimization steps 74% of maximum stress of the initial specimen remains and further reduces to only 67% after  $n = 5$  steps. For comparison, the stress distributions in the specimen from Finite Element simulation are shown for the steps  $n = 0$  and  $n = 5$ . With increasing  $n$  a homogeneous range at center appears, too.

The probability of cracks in a tapered region of the cross-section decreases significantly with lower notch stresses,<sup>43</sup> allowing undisturbed crack documentation throughout the test.

However, the homogeneity grows only under-proportionally with increasing optimization level. Already with two iterations, the stress ratio is reduced to 74%. In a further two steps, only an additional 7% is then achieved. Simultaneously, the specimen lengthens with each iteration step due to a progressively flatter inclination of the tapering. This is due to the method of tension triangles and

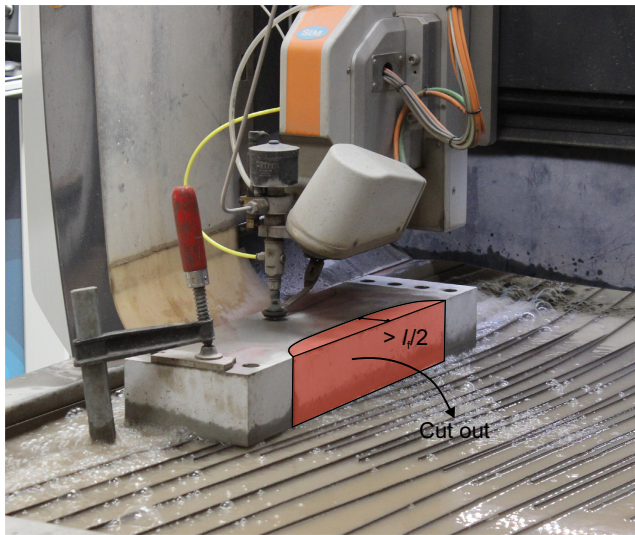


FIGURE 3 Specimen during water jet cutting

the restriction that a constant tensile zone of 10 cm must strictly be maintained. Initially, the specimen measures 45 cm; with  $n = 5$  iteration steps it lengthens to about 72 cm. A limitation is therefore the maximum allowable length in the testing machine. For our purpose, the optimization is terminated after  $n = 5$  iteration steps and the specimen is transferred to a 3D computer-aided design model (CAD model).

After the rectangular concrete specimens have hardened, they are reshaped by water jet cutting (STM PremiumCut) (Figure 3). Reading the CAD file generated from the optimization directly into the system enables accurate cutting. Figure 3 shows a specimen in the cutting machine.

### 3 | TEST SETUP

#### 3.1 | Idea

In contrast to other material tests such as bending or splitting tensile tests, tensile tests set high demands on the equipment, the measurement technology and the testing device. Due to material inhomogeneity, a conversion from the cylindrical compressive strength anchored in EN 1992-1-1/NA<sup>44,45</sup> is used to determine the tensile strength of normal strength concrete. Alternatively, splitting tensile tests are performed. For the determination of the residual flexural tensile strength of SFRC, notched three-point bending tests are mostly performed according to EN 14651.<sup>46</sup> In Germany, unnotched four-point bending tests are carried out on the basis of the guideline “Steel Fiber Reinforced Concrete” of the German Committee for Structural Concrete.<sup>47</sup> From the force-

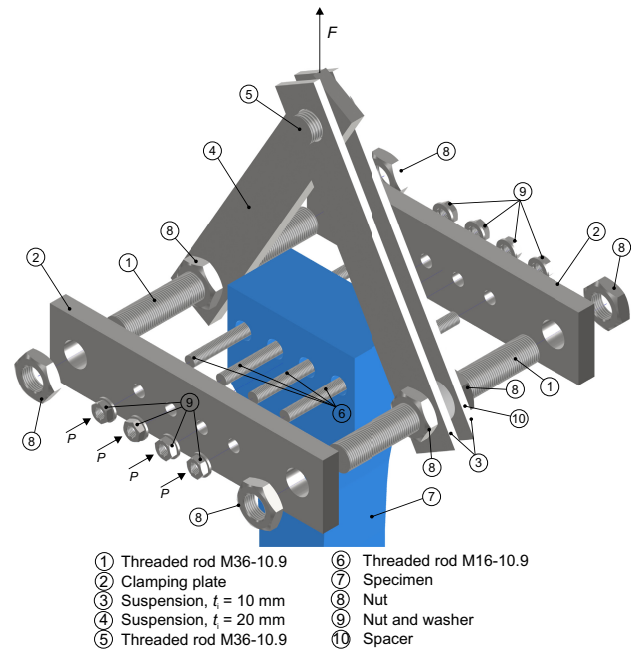


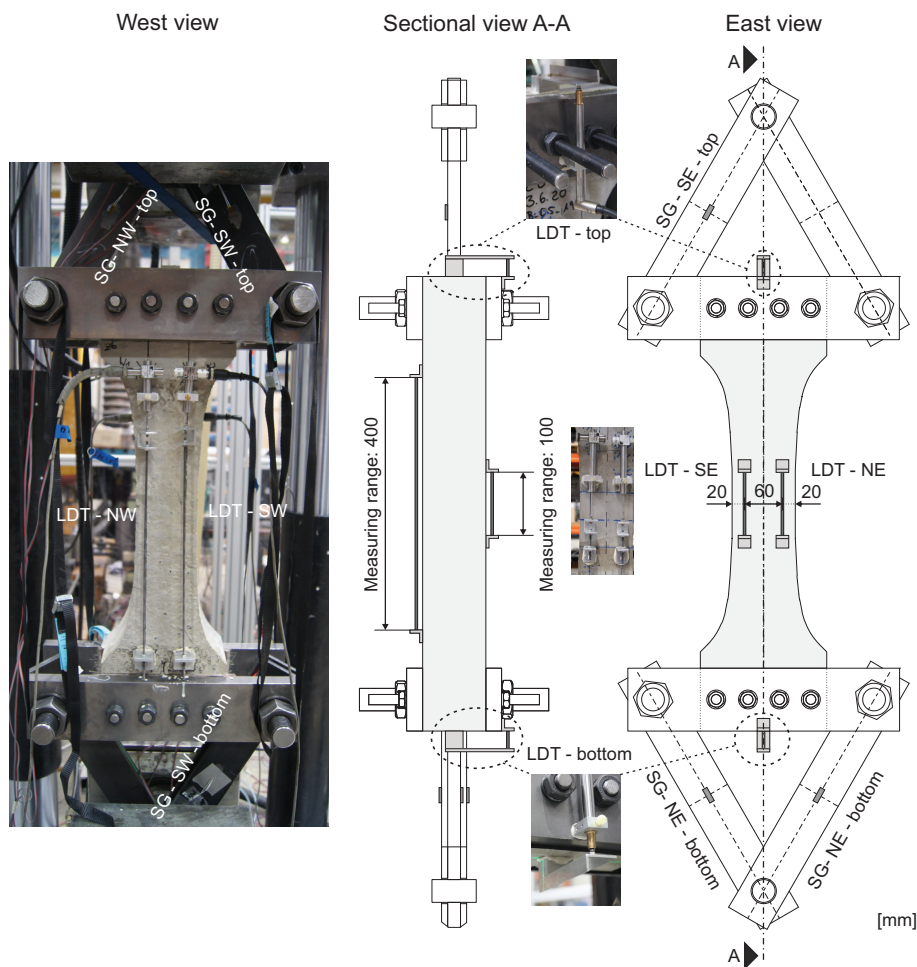
FIGURE 4 Exploded assembly drawing of the upper load application for the tensile tests

deformation relation, individual crack mouth opening displacements (CMOD) for the three-point bending test and deflections for the four-point bending test at small deformations in the serviceability limit state as well as for large deformations in the ultimate limit state (ULS) are derived. The conversion of the residual flexural tensile strengths into centric residual tensile strengths is performed analogously for both configurations. Simplifying assumptions are made regarding the height of the compression zone and the stress distributions in the compressive and tensile zones of the cross-section. In favor of constant conversion factors, the influence of the residual tensile strength on the compression zone height is neglected. However, for a realistic design of steel fiber reinforced components, directly determined tensile strengths are required, since they are more accurate. For this reason, a test rig, specially adapted to the specimen presented above, was developed for axial tensile tests. Six tensile specimens were tested on this rig (S1–S6). The results of six beams (B1–B6) of the same material subjected to four-point bending are used for comparison.

#### 3.2 | Assembly and measurement instrumentation

The load introduction consists of two identical components. The upper one is shown in Figure 4; a general view is presented in Figure 5. The threaded rod at the top (5) is clamped in the hydraulic jaws of the testing

FIGURE 5 Assembly of the test rig and installation of measurement instrumentation



machine. From there, the load is transferred in a truss-like manner via two 10 mm thick plates (3) or one 20 mm thick plate (4), respectively. These plates transfer the load evenly to two lateral threaded rods (1) and into clamping plates (2). By friction, the force is then introduced into the test specimen (7) clamped with four threaded rods (6). Before testing, the test specimen is centered with nuts (8, 9) and a cross-line laser. Prestressing of 50 kN per rod is applied alternately by means of a torque wrench. The clamping plates are coated on the inside with an epoxy resin-corundum mix to ensure enough friction. Geometrical data for the individual components are given in Figure 4. A special feature is that the clamping plates are of variable design so that  $b = 10$  to 20 cm wide and  $h = 5$  to 15 cm deep specimens fit inside. The maximum test load of the test rig is 150 kN and thus reliably covers the practically relevant range.

Crack opening in the central region is measured by four displacement transducers—two on the front and two on the back of the specimen. Two displacement transducers (LDT-SE, LDT-NE; Figure 5) measure crack opening over the constant cross-sectional area of 10 cm length. On the opposite side, two displacement transducers (LDT-

SW, LDT-NW; Figure 5) span the entire length of the tapering of  $\sim 40$  cm. Here, despite the optimization-related uniform stress utilization, unevenness may have been caused by the waterjet cutting, which causes cracking away from the central constant area. Six strain gauges (LDTs) on the outer surface of the truss-like steel structure control the uniform load distribution of the test setup. Two additional LDTs measure the relative motion between the specimen and the clamping plates (LDT-top, LDT-bottom) and control the slip.

The tensile tests are carried out with a servohydraulic compression/tension testing device, which can apply a maximum static force of 1000 kN. The tests are displacement-controlled and run at a speed of 0.1 mm/min.

## 4 | RESULTS

### 4.1 | Qualification of the specimen

The quality of the cut surfaces is evaluated using a 3D scanner based on digital fringe projection (ATOS

Compact Scan, GOM GmbH). It is used to scan the specimen while the integrated software converts the scan into a polygon mesh (actual data). The 3D CAD model of the bone-shaped specimen and the scanned data are aligned with each other using the GOM Inspect Suite software at reference points by the least squares method (residual sum of squares [RSS] of CAD data and scan is minimized). The software computes the perpendicular distances of each reference point of the actual data-set to the target CAD data-set. A spatial comparison for the entire specimen is shown in Figure 7 while Figure 9 presents a detail at the clamping. In blue regions, the measured surface lies above the targeted CAD surface (specimen too large). In red regions, the actual data are below the targeted CAD surface—too much material was removed. Green highlights the wide area with almost no deviations.

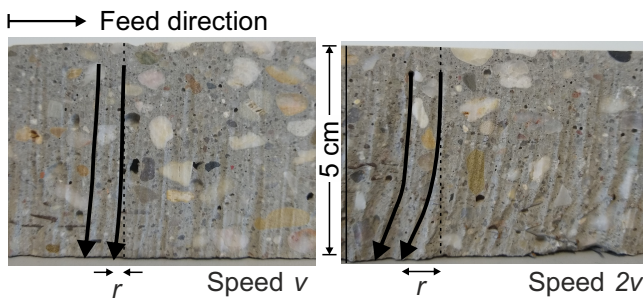


FIGURE 6 Doubled speed significantly increases groove tracking

### 4.1.1 | Quality of the cuts

Due to the large thickness of 10 cm and the inhomogeneous material, an abrasive cutting jet is selected.<sup>48</sup> Fine-grained garnet sand is added to the high-pressure water jet. During cutting the cutting jet pushes overburden material ahead. Due to friction it loses energy with increasing penetration depth,<sup>48</sup> so that it drifts away and yields distinct trailing grooves. The higher the cutting speed, the greater the cutting radius and the thicker the material, the greater the groove tracking and the depth

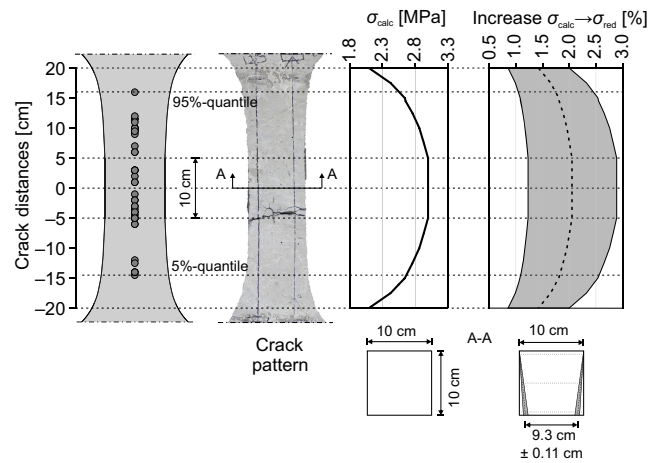


FIGURE 8 Crack pattern and distances from the center along with 5%- and 95%-quantiles and calculated stress over the section with and without consideration of roughness scatter

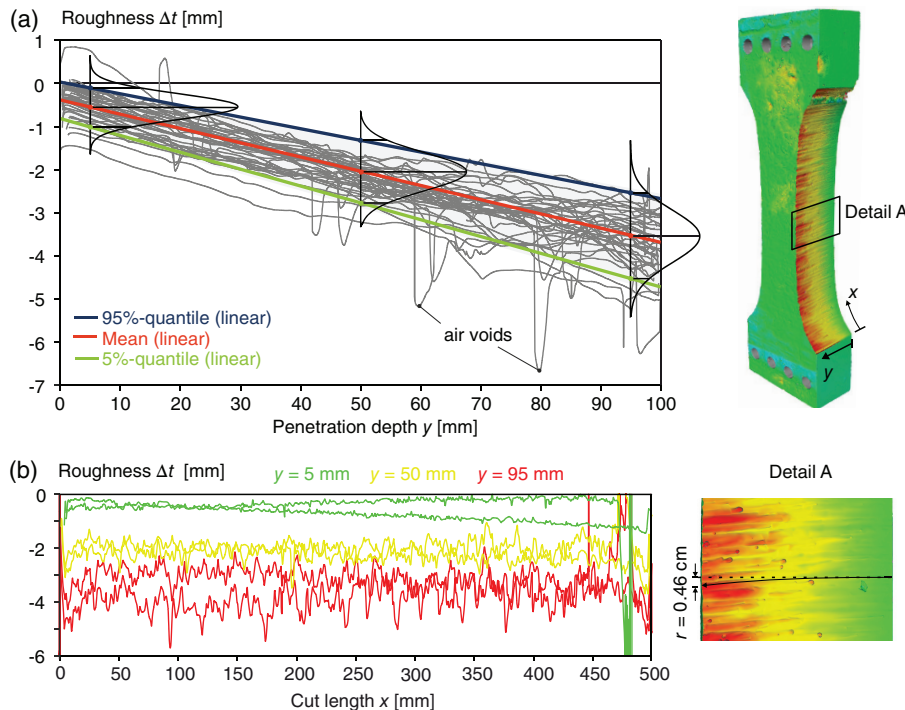
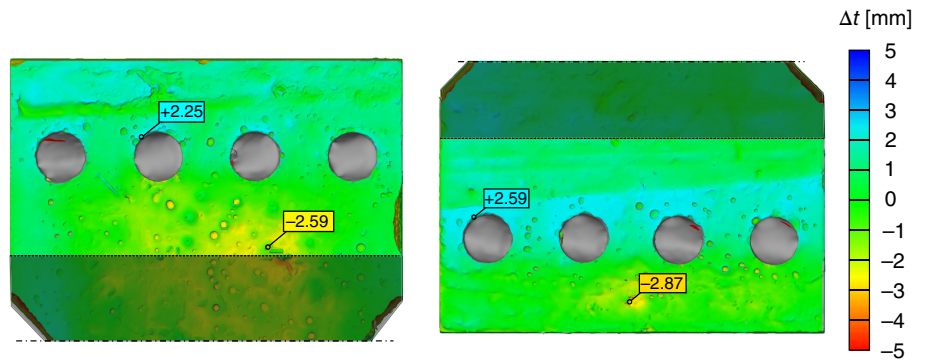


FIGURE 7 Roughness  $\Delta t$  (mm) as a function of the penetration depth  $y$  in direction of cutting  $x$  (a) and roughness profiles in direction of cutting  $x$  for both edges and penetration depths of 5, 50, and 95 mm (b).

FIGURE 9 Roughness near the clamping

TABLE 1 Groove lag  $r$  dependent on the cutting speed  $v$ 

$v$ (mm/min)	$r$ (cm)
15	0.27
36.6	0.88

and width of the grooves are. In concrete construction, waterjet cutting technology is mainly used to repair reinforced concrete structures and to uncover bar reinforcement, so up to now there is very little experience in cutting concrete using waterjet cutting—in contrast to steel. Prior to the actual tests, preliminary tests were performed on 5 cm thick slabs, which have shown the influence of the cutting speed on the quality of the cutting surface. The result is shown in Figure 6. On the left, cutting is performed at an average speed of  $v = 15$  mm/min (Table 1). On the right, the speed is more than doubled (36.6 mm/min). The groove lag  $r$  increases significantly and triples (Table 1). Likewise, the roughness increases with the penetration depth. The grooves become wider and deeper. This becomes even more pronounced on a 10 cm thick specimen. The speed must consequently be low which significantly increases the duration of the cutting process. Advantages of waterjet cutting compared with other cutting techniques such as laser or plasma cutting are the high variability regarding the material, the maximum component thickness as well as the possibility to cut composites made of different materials—such as SFRC.<sup>49</sup> Since hardly any heat is generated during waterjet cutting, no thermally induced changes in the material parameters occur.<sup>49</sup> An influence on the tensile strength can be excluded.

#### 4.1.2 | Roughness of the cutting edges

Figure 7 shows the roughness profiles  $\Delta t$  (mm) of the two cutting edges over the penetration depth  $y$  (Figure 7a) and in direction of cutting  $x$  (Figure 7b). In Figure 7a, 20 cuts

TABLE 2 Mean roughness  $\mu$ , standard deviation (SD)  $\sigma$  as well as 5%- and 95%-quantiles in direction of cutting for penetration depths of  $y = 5, 50,$  and  $95$  mm

$y$ (mm)	5	50	95
Mean $\mu$ (mm)	-0.52	-2.10	-3.50
SD $\sigma$ (mm)	0.32	0.44	0.68
5%-quantile (mm)	-1.05	-2.83	-4.62
95%-quantile (mm)	0.00	-1.36	-2.38

per edge at a distance of  $x = 25$  mm to each other are shown as gray curves. For both edges the roughness profiles  $\Delta t$  in direction of cutting  $x$  have been prepared in Figure 7b at penetration depths of 5 (green), 50 (yellow), and 95 mm (red).

Two things can be observed. First, as the penetration depth increases, the roughness increases almost constantly (Figure 7a). Likewise, the oscillation in the roughness profiles increases (Figure 7b).

For the curves shown in Figure 7b, Table 2 lists the means  $\mu$ , standard deviations  $\sigma$  as well as 5%- and 95%-quantiles over both cutting surfaces for the three penetration depths  $y = 5, 50,$  and  $95$  mm. These are then integrated as colored lines in Figure 7a (green: 5%-quantile, red: mean, blue: 95%-quantile) as a function of the penetration depth  $y$ . Assuming a normally distributed roughness  $\Delta t \rightarrow N(\mu, \sigma^2)$  with variance  $\sigma^2$ , the density functions derived from the characteristic values listed in Table 2 are plotted in Figure 7a.

With increasing penetration depth, both the expected value (red curve, Figure 7a, Table 2) and the standard deviation as a measure of dispersion increase. The density widens, that is, the distance between the 5%- and 95%-quantiles increases. This can also be seen in Figure 7b, where the oscillation of the roughness increases with the penetration depth. While at a penetration depth of  $y = 5$  mm the averaged roughness of both cutting edges is still  $\Delta t = -0.52$  mm (Table 2), at a penetration depth of  $y = 95$  mm it increases to

Crack distance (cm)	5%-quantile (%)	Mean (%)	95%-quantile (%)
+16.0 (95%-quantile)	2.4	1.7	1.0
0	2.9	2.1	1.2
-14.5 (5%-quantile)	2.5	1.8	1.1

TABLE 3 Stress increase due to trapezoidal cross-section and roughness scatter along the specimen

$\Delta t = -3.50$  mm on average. 90% of all deviations at a penetration depth of 5 mm lie between 0 and  $-1.05$  mm. At a penetration depth of  $y = 95$  mm, this range increases from  $-2.4$  to  $-4.6$  mm. The few exceptions are mainly caused by grains not cut by the water jet. The groove lag (calculated:  $r = 0.46$  cm) is low due to the slow cutting speed (Figure 7).

The offset between the top and bottom edge yields a trapezoidal cross-section. Therefore, cracks occur outside the predefined range of 10 cm at center, too. Next to an exemplary crack pattern, the crack distances from the center are shown for all tests on the left in Figure 8. From these the 5%- and 95%-quantiles are calculated to  $-14.5$  and  $16$  cm, respectively. On average the crack forms at a distance  $\pm 7.3$  cm from the center.

Both, trapezoidal cross-section and scatter of the roughness are considered in the prediction of stresses. At a cross-section of  $10 \times 10$  cm<sup>2</sup> and a maximum load of 30 kN Figure 8 shows the calculated stresses  $\sigma_{\text{calc}}$  as well as the stress increase to  $\sigma_{\text{red}}$ . At the same load level  $\sigma_{\text{red}}$  denotes the stresses at the trapezoidal cross-section reduced by roughness. For the center of the specimen, an average stress increase of 1.2%–2.9% is found (Table 3). For the two quantiles the increase is even smaller. Thus, the error due to calculation on a cross-section of  $10 \times 10$  cm<sup>2</sup> is on the safe side, smaller than 3% and negligible.

#### 4.1.3 | Clamping device at the load introduction

Distinct roughness can be seen around the clamping of the specimen (Figure 9). Air voids have risen during compaction of the concrete that are now clearly visible. They are attributed to insufficient smoothing of the concrete. Since the PVC tubes were precisely aligned and fixed in the formwork as recess units, the concrete could not be cured. Figure 9 highlights the maximum and minimum deviations that have occurred near the clamping (unshaded region,  $h = 10$  cm). The maxima (blue) occur at the edges of the recess units. The cause is again the PVC pipes. A layer of cement paste up to 2.6 mm thick has accumulated there. Other, punctual deviations (yellow) are due to air voids from compaction that could not be smoothed due to limited accessibility. They amount to

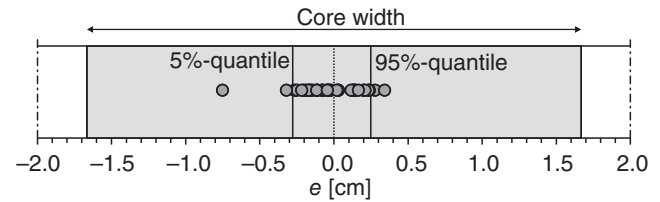


FIGURE 10 Back-calculated eccentricities of load application at cracking

2.9 mm at maximum. The consequence is uneven clamping. And during clamping, this leads to cracks caused by local stress peaks in the specimen. Increasing prestressing leads to minor surface spalling of the concrete (Figure 9, left) until finally 50 kN per threaded rod are reached. Due to the then complete prestressing, the concrete is fully compressed around the clamping. An impact on the stress–crack opening relationship must thus not be assumed. Widening of the cracks initiated by prestressing is not observed during the tests. An influence on the residual tensile strength can therefore be discarded.

A potential improvement to the provision of holes through tubes would be their subsequent drilling, which would allow concrete smoothing. Furthermore, the coating of the clamping plates with corundum and epoxy resin proved to be insufficiently elastic. It should be made less stiff so that it can compensate for minor unevenness and evenly transfer the stresses into the concrete.

## 4.2 | Qualification of the test set-up

### 4.2.1 | Eccentricity

Centric load introduction into the specimen is essential to determine the tensile strength. The specimen shall not experience any bending due to unwanted eccentricity of the load. This is checked by strain gauges attached to the diagonals, which are used to control the stress in the struts and thus the distribution of the loads. The eccentricities recalculated from strains are shown as gray dots in Figure 10. If the load application lies within the core width of a cross-section only stresses of one sign occur. For the rectangle, it is calculated as:  $h/6 = 10/6 = 1.67$  cm (shown in light gray). The mean eccentricity recalculated from the

strains at the time of cracking is determined to be  $e = 1.6$  mm and makes only one tenth of the core width. All back-calculated eccentricities fall safely within this computational limit. Even more, the labeling of the 5%- and 95%-quantiles proves a consistently low scatter and shows that even these scatter limits, quite common in engineering, have still a significant distance from the computational limit. Thus, the cross-section is fully in tension at the time of cracking. The eccentricities found thus are negligible with respect to the tensile strength.

#### 4.2.2 | Slip

Dependent on the crack opening, Figure 11 shows the displacements of the LDTs in micrometers, which are attached to one of the upper (black) or lower (gray) clamping plates of the test setup (cf. Figure 5). They measure the relative displacement between the specimen and the clamping plate that is henceforth referred to as slip. In total, six tensile specimens (S1–S6) were examined. Crack openings are characterized by discontinuities in the course, since the load redistribution in the specimen, due to the plane fiber orientation and its uniform distribution, causes minimal slipping. Most LDTs reach a constant plateau after cracking. This is seen as an indicator that the test rig allows such small micrometer-scale

movements without introducing constraint into the specimens. Only three curves show no plateau. These are the two LDTs of S6 and that of the lower LDT of S4 (Figure 11). In these cases, the adhesive to attach the LDT has not had hardened sufficiently (cf. Figure 5). The LDTs fell off during testing and the associated measurements were lost to assess the slip. If available at all the recordings are put into brackets in Table 4. Similar applies to the lower LDT of S3 that failed before the experiment had started. Its curve is missing in Figure 11. According to Equation (1), the maximum slip at which the prestressed threaded rods would come into contact with the concrete surface and thus induce constraint is obtained to half the distance from the outside of the threaded rod of  $d_t = 16$  mm to the concrete surface in the hole with a diameter of  $d_o = 25$  mm.

$$\frac{d_o - d_t}{2} = \frac{25 - 16}{2} = 4.5 \text{ mm} = 4500 \mu\text{m} \quad (1)$$

The measured slip of both LDTs at the top and bottom (cf. Figure 5) at cracking is listed for all specimens in Table 4. In all cases, it remains well below the limit at which constraint would be induced. Even after cracking, no slip exceeds  $6 \mu\text{m}$ . Consequently, constraint is indeed no reason for the failure of LDTs or the lack of plateau formation.

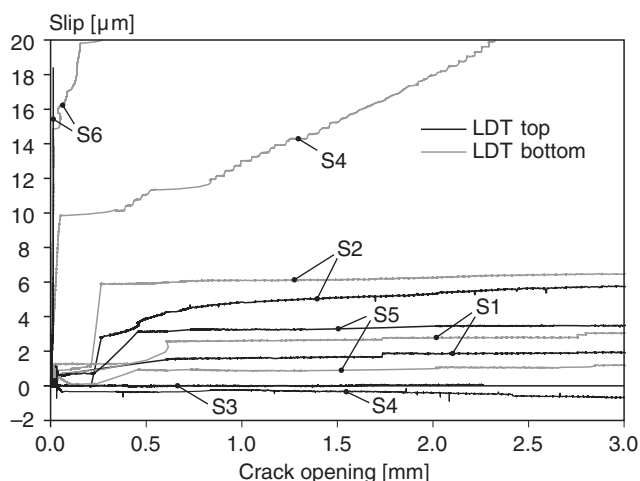


FIGURE 11 Relative displacement of the specimen to the test rig at top and bottom as a function of crack opening

#### 4.3 | Stress–crack opening relationship

Figure 12a shows on the primary ordinate the stress–crack opening relationships of the six tensile tests (gray curves) and their mean value (black curve). On the secondary ordinate, the coefficient of variation (COV) is shown as a measure of dispersion (dashed curve). Figure 12b shows the force–deflection relationships of the six beams (B1–B6) made with the same concrete mix in the four-point bending test (gray curves) and their mean value (black curve) on the primary ordinate. Deflection at mid-span  $\delta$  is calculated as a mean out of the two measured LDTs (cf. Figure 12b) according to DAfStb-Guideline.<sup>47</sup> The COV is again plotted on the secondary ordinate (dashed curve). The beam experiments are described in detail in Look et al.<sup>17</sup>

TABLE 4 Maximum slip of specimen at top and bottom at cracking in ( $\mu\text{m}$ )

	S1	S2	S3	S4	S5	S6
LDT-top ( $\mu\text{m}$ )	0.84	0.52	0.08	0.16	1.86	(18.39)
LDT-bottom ( $\mu\text{m}$ )	0.74	0.91	—	(9.84)	1.25	(14.85)

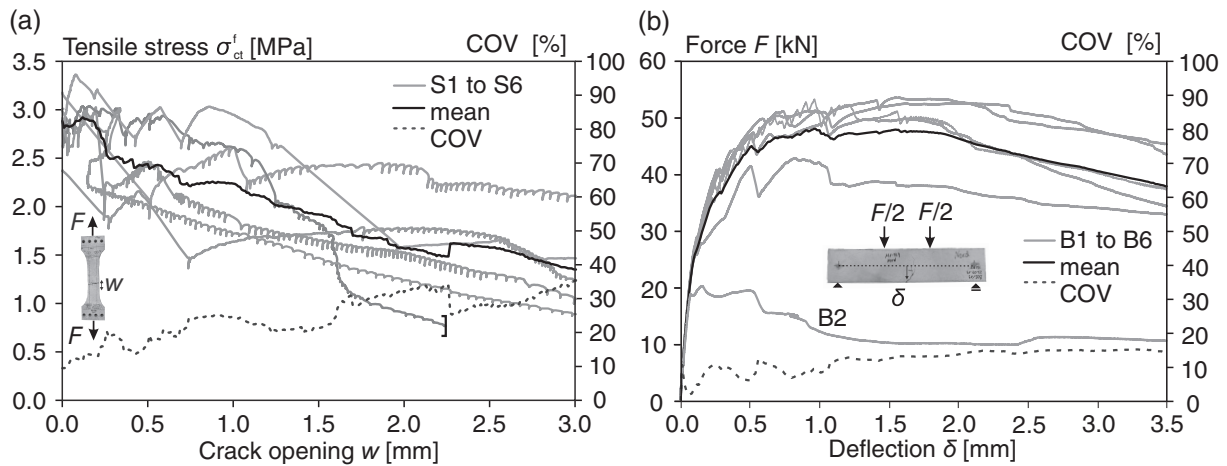


FIGURE 12 Stress–crack opening relationships of the tensile tests (a) and load–deflection curves of the bending tests (b) along with means and coefficient of variation.

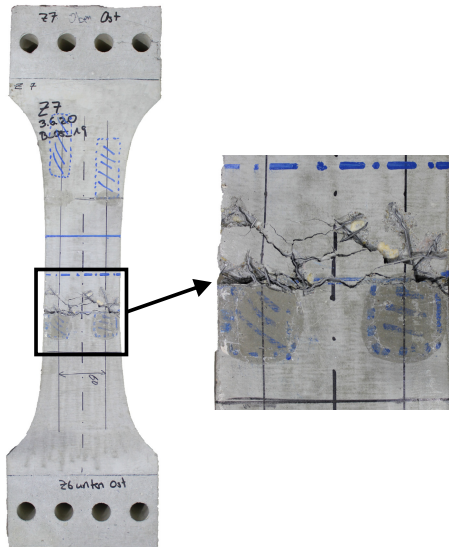


FIGURE 13 Specimen after testing and crack pattern at center

To determine the crack opening, the mean value of the two displacement transducers applied to the west of the tensile specimens is evaluated over a measuring length of 40 cm (Figure 5, LDT-NW and LDT-SW). The fixations of the eastern displacement transducers with a measuring length of 10 cm detached several times during the tests, so that there is no sufficient amount of data for a stable mean prediction. The reason for this was almost exclusively (micro)-crack formation, which led to the loosening of the adhesive.

The macrocrack finally formed on average at a distance of  $\pm 7.3$  cm from the center of gravity (i.e., up to 2.3 cm outside the targeted crack area with constant cross-section). The homogeneous stresses in the specimen

in combination with the two-sided unevenness of in total  $2 \times 3.5 = 7$  mm resulted in specimen being only  $93 \pm 1.1$  mm wide in some places and thus cracks also formed outside the advised measuring range.

All specimens remained in one piece after testing and when removed from the testing device and did not break, as the steel fibers were able to bridge the cracks (Figure 13). The ductile, yet softening postcracking behavior is clearly evident in the stress–crack opening relationship (cf. Figure 12). After cracking, the force steadily decays in a controlled manner. Discontinuities in the diagrams indicate the branching of the macrocracks and the continuous widening of the macrocrack. Even before the first macrocrack forms, several smaller (micro)-cracks develop, which then join to an opening crack. The characteristic crack pattern of our six test specimens as exemplified in Figure 13 shows multiple cracking with branched individual cracks as typical for SFRC.

Table 5 summarizes the evaluation of the tensile and bending tests and shows the mean value of the (flexural) tensile strength, its standard deviation and the COV for  $\text{CMOD}_1$ ,  $\text{CMOD}_3$ , and the maximum force.

The conversion of the deflection  $\delta$  from the four-point bending test into equivalent  $\text{CMOD}$ s of the three-point bending test is based on EN 14651<sup>46</sup> and accounts for the different spans of the two tests with Equation (2).<sup>13,50</sup>

$$\text{CMOD} = 0.98\delta - 0.047 \quad (2)$$

The average measured value of the maximum tensile strength after cracking  $f_{ct,max}$  is 2.87 MPa. Crack load  $f_{ct,cr}$  scatters only by  $\text{COV} = 11\%$  (Table 5). However, the scatter increases with increasing deformation due to material

**TABLE 5** Mean, standard deviations (SD), and COV of the tensile strength  $f_{ct}^i$ , at  $i = \text{CMOD}_1, \text{CMOD}_3$ , cr for cracking, and max for maximum load after cracking

	Tensile test				Bending test	
	$f_{ct,cr}$	$f_{ct,max}$	$f_{ct,CMOD1}$	$f_{ct,CMOD3}$	$f_{cfI,CMOD1}$	$f_{cfI,CMOD3}$
Mean (MPa)	3.00	2.87	2.44	1.58	7.82	7.60
SD (MPa)	0.33	0.42	0.41	0.43	0.96	1.14
COV (–)	0.11	0.15	0.17	0.27	0.12	0.15

inhomogeneity and the nonuniform initial crack opening over the cross-section. This leads to a bending effect, which, however, only occurs after the initial crack has appeared and thus has no influence on the cracking behavior.

Likewise low scatter ranges of 12% and 15% for  $\text{CMOD}_1$  and  $\text{CMOD}_3$ , respectively, occurred in the bending test. By contrast, in flexural tests with conventional fiber contents up to  $80 \text{ kg/m}^3$ , coefficients of variation of up to 25% can be expected.<sup>51</sup>

The low scatter indicates the suitability of the developed test rig. In particular, it does not favor constraint and prevents bending effects. At the same time, the low scatter proves that the SFRC is consistently of high quality due to its high fiber content and the given manufacturing conditions.

#### 4.4 | Conversion of flexural and tensile results

The conversion of the residual flexural strength  $f_{cfI}$  into a centric residual tensile strength  $f_{ct}$  is usually performed normatively on basis of Equation (3) by means of the conversion factor  $\beta$ . Established conversion factors are throughout based on the assumption of softening post-cracking behavior. How or whether a factor determined from bending tests with hardening material behavior compares to this is examined below.

$$f_{ct} = \beta \cdot f_{cfI} \quad (3)$$

Table 6 lists established conversion factors for a rigid-plastic constitutive law according to the new Eurocode with Annex L,<sup>52</sup> the Model Code 2010<sup>53</sup> and also the German guideline Steel Fiber Reinforced Concrete.<sup>47</sup>

The determination of the residual tensile strength is basically carried out for the ULS at  $\text{CMOD}_3 = 2.5 \text{ mm}$ . By comparing the linear-elastic material behavior in state I with that of state II while preserving the moment, the conversion factors given in Table 6 are obtained.<sup>54</sup> For a conversion factor of  $\beta = 0.33$ —as embodied in the Model Code 2010—this assumes a cross-section fully in tension and a compressive axial force applied exclusively in the uppermost cross-section fiber.<sup>55</sup> For a conversion factor

**TABLE 6** Conversion factors  $\beta$  for a rigid-plastic constitutive law from standards

Standard	$\beta$
prEN 1992-1-1, Annex L <sup>52</sup>	0.37
Model Code 2010 <sup>53</sup>	0.33
DAfStb-Guideline SFRC <sup>47</sup>	0.37

of 0.37, however, a compression zone height of 10% of the whole height is assumed.

For the bending tensile tests published in Look et al.<sup>17</sup> (cf. Figure 12b) and the tensile tests presented here, an identical SFRC mix was used. Likewise, uniform manufacturing conditions prevailed, so that a similar fiber distribution and orientation can be expected in both, that is, a direct conversion of the residual flexural tensile strength to the residual tensile strength seems possible. For this purpose, the maximum tensile strength  $f_{ct,max}$  measured after cracking (Table 5) is divided by the mean residual flexural tensile strength  $f_{cfI,CMOD3}$  determined at  $\text{CMOD}_3 = 2.5 \text{ mm}$ .<sup>56,57</sup> This yields a conversion factor according to Equation (4), which is close to that of prEN 1992-1-1/Annex L and to that in the German guideline (Table 6).

$$\beta_{\text{CMOD}_3} = \frac{f_{ct,max}}{f_{cfI,CMOD_3}} = \frac{2.87}{7.60} = 0.38 \quad (4)$$

## 5 | CONCLUSIONS

At first, a method to produce bone-shaped, shape-optimized tensile specimens made from SFRC and to eliminate the parasitic lateral wall effect typical for the material, which increases the load-bearing capacity, was presented and qualified. Moreover, a test rig to directly determine the tensile strengths of SFRC with supercritical fiber content was developed and qualified. The results of six tensile tests were evaluated and compared with the results from flexural tensile tests of the same SFRC. Finally, a conversion factor to derive tensile strengths

from flexural strengths could be obtained and compared with those in standards. The following conclusions are drawn:

- Optimization of the specimen shape and an adaptation to real conditions regarding fiber orientation and systematic elimination of the wall effect enable to determine realistic tensile strength directly.
- Waterjet cutting permits to cut an optimum-shaped concrete specimen precisely without any formwork effort. The roughness of the cutting surfaces increases with the penetration depth of the jet. From  $-0.52$  mm on average at a depth of 5 mm it increases to  $-3.50$  mm at a depth of 95 mm. It provides sufficient accuracy of the cutting edges. The influence of associated deviations on the tensile strength can be neglected.
- The developed test rig introduces the load centrally into the tensile specimen and imposes neither unwanted bending nor constraint on it. All measured eccentricities are well within the calculated limits of the core width and are negligibly small.
- The prestress of the clamping is so high that the tensile specimen hardly moves relative to the test rig. However, there is potential for improvement in the coating of the clamping plates as well as the curing of the specimens near the clamping in order to gain smooth surfaces and uniform compression.
- The SFRC shows softening behavior in the post-cracking domain subjected to direct tension with an average maximum tensile strength of 2.87 MPa. The specimen does not fail brittle and the crack edges do not separate completely even after the end of the test.
- The conversion factor to determine the tensile from the flexural strength is obtained from the tests to 0.38 and is close to those in standards.
- Variations in the material, fiber content, types and cutting technique may provide further insight into the merits of this method for designing semiprecast concrete elements as (partial) replacements for crosswise laid reinforcement.<sup>2,58,59</sup>
- With the here measured tensile strength of  $f_{ct,max} = 2.87$  MPa,  $\sim 287$  kN/m tensile forces can be born assuming a height of 10 cm. In terms of load bearing capacity, this corresponds to a typical reinforcement ( $f_{yk} = 500$  MPa) of  $5.7$  cm<sup>2</sup>/m per direction. In flat components such as foundations or wall elements, crosswise reinforcement can thus be substituted by a semiprecast member made of SFRC.

## ACKNOWLEDGMENTS

The authors would like to thank BASF SE, BauMineral GmbH, NV Bekaert SA and Dyckerhoff GmbH for the friendly provision of the test materials. Many thanks also

to the members of the Structural Testing Laboratory at Ruhr University Bochum, Germany (<https://www.ruhr-uni-bochum.de/kib-kon/>).

## DATA AVAILABILITY STATEMENT

The data that support the findings of this study are available from the corresponding author upon reasonable request.

## ORCID

Katharina Look  <https://orcid.org/0000-0002-5505-5696>

Peter Mark  <https://orcid.org/0000-0003-1812-2148>

## REFERENCES

1. Mark P, Lanza G, Lordick D, Albers A, König M, Borrmann A, et al. Vom Handwerk zur individualisierten Serienfertigung. *Bautechnik*. 2021;98(3):243–56. <https://doi.org/10.1002/bate.202000110>
2. Mark P, Lanza G, Lordick D, Albers A, König M, Borrmann A, et al. Industrializing precast productions. *Civil Eng Des*. 2021; 3(3):87–98. <https://doi.org/10.1002/cend.202100019>
3. Martinie L, Roussel N. Simple tools for fiber orientation prediction in industrial practice. *Cem Concr Res*. 2011;41(10):993–1000. <https://doi.org/10.1016/j.cemconres.2011.05.008>
4. Schulz M, Oettel V. Verwendung von stahlfaserverstärktem Stahlbeton bei Bodenplatten für automatisierte Hochregallager. *Beton- Stahlbetonbau*. 2021;116(S1):70–6. <https://doi.org/10.1002/best.202100008>
5. Heek P, Tkocz J, Mark P. A thermo-mechanical model for SFRC beams or slabs at elevated temperatures. *Mater Struct*. 2018;51(4):78. <https://doi.org/10.1617/s11527-018-1218-8>
6. Plückelmann S, Breitenbücher R, Smarslik M, Mark P. Aufnehmbare Teilflächenspannung von hochfestem Stahlfaserbeton. *Beton- Stahlbetonbau*. 2019;114(9):653–62. <https://doi.org/10.1002/best.201900015>
7. Putke T, Song F, Zhan Y, Mark P, Breitenbücher R, Meschke G. Entwicklung von hybriden Stahlfaserbetontübbings: Experimentelle und numerische Analysen von der Material- bis zur Bauwerksebene. *Bauingenieur*. 2014;89(11):447–56.
8. Smarslik M, Mark P. Hybrid reinforcement design of longitudinal joints for segmental concrete linings. *Struct Concr*. 2019; 20(6):1926–40. <https://doi.org/10.1002/suco.201900081>
9. Teutsch M. Einsatz von Stahlfaserbeton im Tunnelbau. *Beton- Stahlbetonbau*. 2006;101(5):311–21. <https://doi.org/10.1002/best.200600481>
10. Trabucchi I, Smarslik M, Tiberti G, Petrarola DN, Plizzari GA, Mark P. A hybrid solution proposal for precast tunnel segments. *Struct Concr*. 2021;22(3):1534–48. <https://doi.org/10.1002/suco.202000629>
11. de Waal R. Steel fibre reinforced tunnel segments—For the application in shield driven tunnel linings. Dissertation, Delft University of Technology; 1999.
12. Minelli F, Plizzari GA. On the effectiveness of steel fibers as shear reinforcement. *ACI Struct J*. 2013;110(3):379–89. <https://doi.org/10.14359/51685596>
13. Heek P, Look K, Oettel V, Mark P. Bemessung von Stahlfaserbeton und stahlfaserbewehrtem Stahlbeton. *Beton-*

- Stahlbetonbau. 2021;116(S1):2–12. <https://doi.org/10.1002/best.202100009>
14. Look K, Landler J, Mark P, Fischer O. Fasermengen und Leistungsklassen. *Beton- Stahlbetonbau*. 2021;116(S1):13–23. <https://doi.org/10.1002/best.202100004>
  15. Sorelli LG, Meda A, Plizzari GA. Steel fiber concrete slabs on ground: A structural matter. *Struct J*. 2006;103(4):551–8. <https://doi.org/10.14359/16431>
  16. Sigrist V, Bentz E, Ruiz MF, Foster S, Muttoni A. Background to the *fib* Model Code 2010 shear provisions - part I: beams and slabs. *Struct Concr*. 2013;14(3):195–203. <https://doi.org/10.1002/suco.201200066>
  17. Look K, Heek P, Mark P. Towards rebar substitution by fibres: Tailored supercritical fibre contents. In: Serna P, Llano-Torre A, Martí-Vargas JR, Navarro-Gregori J, editors. *Fibre reinforced concrete—improvements and innovations: RILEM-fib international symposium on FRC (BEFIB) in 2020*. Cham: Springer; 2021. p. 908–19.
  18. Jungwirth J. Zum Tragverhalten von zugbeanspruchten Bauteilen aus Ultra-Hochleistungs-Faserbeton. Dissertation, Technical University of Munich; 2006.
  19. Tipka M, Vašková J, Vodička J. Tensile strength tests for concrete and fibre reinforced concrete. *Solid State Phenomena*. 2018;272:94–101.
  20. Wille K, El-Tawil S, Naaman AE. Properties of strain hardening ultra high performance fiber reinforced concrete (UHP-FRC) under direct tensile loading. *Cem Concr Compos*. 2014; 48:53–66. <https://doi.org/10.1016/j.cemconcomp.2013.12.015>
  21. RILEM TC162-TDF. Test and design methods for steel fibre reinforced concrete: uni-axial tension test for steel fibre reinforced concrete. *Mater Struct*. 2001;35:3–6.
  22. Oettel VV. Torsionstragverhalten von stahlfaserbewehrten Beton-, Stahlbeton- und Spannbetonbalken. Dissertation, Technical University of Braunschweig; 2016.
  23. van Mier J, van Vliet M. Uniaxial tension test for the determination of fracture parameters of concrete: State of the art. *Eng Fract Mech*. 2002;69(2):235–47. [https://doi.org/10.1016/S0013-7944\(01\)00087-X](https://doi.org/10.1016/S0013-7944(01)00087-X)
  24. Frettlöhr B. Bemessung von Bauteilen aus ultrahochfestem Faserfeinkornbeton (UHFFB). Dissertation, University of Stuttgart; 2011.
  25. Abrishambaf A, Barros JA, Cunha VM. Relation between fibre distribution and post-cracking behaviour in steel fibre reinforced self-compacting concrete panels. *Cem Concr Res*. 2013;51:57–66. <https://doi.org/10.1016/j.cemconres.2013.04.009>
  26. Hadl P, Gröger J, Tue NV. Experimentelle Untersuchungen zur Streuung im Zugtragverhalten von Stahlfaserbeton. *Bautechnik*. 2015;92(6):385–93. <https://doi.org/10.1002/bate.201500008>
  27. Švec O, Žirgulis G, Bolander JE, Stang H. Influence of formwork surface on the orientation of steel fibres within self-compacting concrete and on the mechanical properties of cast structural elements. *Cem Concr Compos*. 2014;50:60–72. <https://doi.org/10.1016/j.cemconcomp.2013.12.002>
  28. Bantia N, Trottier J-F. Concrete reinforced with deformed steel fibers, part I: bond-slip mechanisms. *ACI Mater J*. 1994; 91(5):435–46. <https://doi.org/10.14359/4059>
  29. Soroushian P, Lee C-D. Distribution and orientation of fibers in steel fiber reinforced concrete. *Mater J*. 1990;87(5):433–9. <https://doi.org/10.14359/1803>
  30. Blanco A, Pujadas P, La Fuente A d, Cavalaro S, Aguado A. Assessment of the fibre orientation factor in SFRC slabs. *Compos B Eng*. 2015;68:343–54. <https://doi.org/10.1016/j.compositesb.2014.09.001>
  31. Mattheck C, Kappel R, Sauer A. Shape optimization the easy way: the method of tensile triangles. *Int J Des Nat Ecodynam*. 2007;2(4):301–9. <https://doi.org/10.2495/D&N-V2-N4-301-309>
  32. Mattheck C, Tesari I, Sauer A, Bethge K, Kraft O. A simple graphic way to reduce stress concentrations by growth. In: Brebbia CA, editor. *Design and nature IV: comparing design in nature with science and engineering*. Southampton, UK: WIT Press; 2008. p. 79–85.
  33. Forman P, Gaganelis G, Mark P. Optimierungsgestützt entwerfen und bemessen. *Bautechnik*. 2020;97(10):697–707. <https://doi.org/10.1002/bate.202000054>
  34. Mattheck C. Design and growth rules for biological structures and their application to engineering. *Fatigue Fract Eng Mater Struct*. 1990;13(5):535–50. <https://doi.org/10.1111/j.1460-2695.1990.tb00623.x>
  35. Mattheck C. Engineering components grow like trees. *Materwiss Werksttech*. 1990;21(4):143–68. <https://doi.org/10.1002/mawe.19900210403>
  36. Belhouil M. Analyse et modélisation du comportement d'un matériau à matrice cimentaire fibrée à ultra hautes performances. Dissertation, Cachan: École normale supérieure Paris-Saclay; 1996.
  37. Dupont D. Modelling and experimental validation of the constitutive law ( $\sigma$ - $\epsilon$ ) and cracking behaviour of steel fibre reinforced concrete. Dissertation, Katholieke Universiteit Leuven; 2003.
  38. Dupont D, Vandewalle L. Distribution of steel fibres in rectangular sections. *Cem Concr Compos*. 2005;27(3):391–8. <https://doi.org/10.1016/j.cemconcomp.2004.03.005>
  39. Kameswara RC. Effectiveness of random fibres in composites. *Cem Concr Res*. 1979;9(6):685–93. [https://doi.org/10.1016/0008-8846\(79\)90063-2](https://doi.org/10.1016/0008-8846(79)90063-2)
  40. Harzheim L. *Strukturoptimierung: Grundlagen und Anwendungen*. 1st ed. Frankfurt am Main: Wissenschaftlicher Verlag Harri Deutsch; 2008.
  41. Mattheck C. *Design in nature: learning from trees*. Berlin, Heidelberg: Springer; 1998.
  42. Gaganelis G, Tkocz J, Smarslik M, Mark P. Konsekutive Wandlung massiger Betonstrukturen in topologisch optimierte Fachwerke. In: Tautschnig A, editor. *Festschrift anlässlich des 60. Breitenbücher: Geburtstages von Herrn Prof*; 2017.
  43. Thum A, Petersen C, Svenson O. *Verformung, Spannung und Kerbwirkung*. Düsseldorf: VDI-Verlag; 1960.
  44. DIN EN 1992-1-1:2011-01: Eurocode 2: Design of concrete structures - Part 1-1: General rules and rules for buildings; German version EN 1992-1-1:2004+AC:2010. Berlin: Beuth; 2011.
  45. DIN EN 1992-1-1/NA:2013-04: National Annex - National determined parameters - Eurocode 2: Design of concrete structures - Part 1-1: General rules and rules for buildings. Berlin: Beuth; 2013.
  46. DIN EN 14651:2007-12: Test method for metallic fibre concrete - Measuring the flexural tensile strength (limit of proportionality (LOP), residual); German version EN 14651:2005+A1:2007. Berlin: Beuth; 2007.
  47. Deutscher Ausschuss für Stahlbeton (DAfStb). *DAfStb-Guideline steel fiber reinforced concrete*. Berlin: Beuth; 2021.

48. Fritz AH, Förster R, Hoffmeister W, Kühn K-D, Schulze G. Trennen. In: Fritz AH, Schulze G, editors. *Fertigungstechnik*. 11th ed. Berlin: Springer; 2015. p. 273–428.
49. Klocke F, König W. *Fertigungsverfahren: Band 3: Abtragen, Generieren und Lasermaterialbearbeitung*. 4th ed. Berlin: Springer; 2007.
50. Weber F, Anders S. Vergleich von 3-Punkt- und 4-Punkt-Biegezugversuchen zur Bestimmung der Nachrissbiegezugfestigkeit. *Beton- Stahlbetonbau*. 2021;116(S1):48–58. <https://doi.org/10.1002/best.202100013>
51. Heek P, Look K, Minelli F, Mark P, Plizzari GA. Datenbank für querkräftbeanspruchte Stahlfaserbetonbauteile. *Beton- Stahlbetonbau*. 2017;112(3):144–54. <https://doi.org/10.1002/best.201600075>
52. prEN 1992-1-1. Annex L to EN 1992-1-1 (Draft D7); 2021.
53. International Federation for Structural Concrete. *fib Model Code for concrete structures 2010*. 1st ed. Berlin: Ernst & Sohn; 2013.
54. Di Prisco M, Plizzari G, Vandewalle L. Fibre reinforced concrete: new design perspectives. *Mater Struct*. 2009;42(9):1261–81. <https://doi.org/10.1617/s11527-009-9529-4>
55. Di Prisco M, Colombo M, Dozio D. Fibre-reinforced concrete in *fib Model Code 2010*: principles, models and test validation. *Struct Concr*. 2013;14(4):342–61. <https://doi.org/10.1002/suco.201300021>
56. Leutbecher T, Rebling J. Predicting the postcracking strength of ultra-high performance fiber reinforced concrete by means of three-point bending tests according to EN 14651. *Struct Concr*. 2019;20(6):2081–95. <https://doi.org/10.1002/suco.201900070>
57. Gödde L, Strack M. Conversion factors for the determination of the tensile behaviour of steel fibre reinforced concrete from bending tests. In: Gettu R, editor. 7th International RILEM symposium on fibre reinforced concrete: design and applications: BEFIB 2008; Indian Institute of Technology Madras, Chennai, India, 17–19 September 2008. Bagnaux: RILEM Publ; 2008. p. 409–18.
58. Forman P, Penkert S, Mark P, Schnell J. Design of modular concrete heliostats using symmetry reduction methods. *Civil Eng Des*. 2020;2(4):92–103. <https://doi.org/10.1002/cend.202000013>
59. Frey AM, Stindt J, Lanza G, Mark P. Geometrische Bewertung und Optimierung der Modulordnung in Tragwerken. *Bautechnik*. 2021;98:662–70. <https://doi.org/10.1002/bate.202100027>

## AUTHOR BIOGRAPHIES



Katharina Look,  
Institute of Concrete Structures,  
Faculty of Civil and Environmental  
Engineering, Ruhr University  
Bochum, Universitätsstraße 150,  
44801 Bochum, Germany.  
katharina.look@rub.de



Peter Mark,  
Institute of Concrete Structures,  
Faculty of Civil and Environmental  
Engineering, Ruhr University  
Bochum, Universitätsstraße 150,  
44801 Bochum, Germany.  
peter.mark@rub.de

**How to cite this article:** Look K, Mark P. Steel fiber reinforced concrete tensile testing with eliminated lateral wall effect. *Structural Concrete*. 2022;23(6):3483–96. <https://doi.org/10.1002/suco.202100831>